Microseismic studies of an underground site for a new interferometric gravitational wave detector

2014 Class. Quantum Grav. 31 105016

(http://iopscience.iop.org/0264-9381/31/10/105016)

IOP Publishing Classical and Quantum Gravity
Class. Quantum Grav. **31** (2014) 105016 (20pp) doi:10.1088/0264-9381/31/10/105016

Microseismic studies of an underground site for a new interferometric gravitational wave detector

L Naticchioni[1,2], M Perciballi[2], F Ricci[1,2], E Coccia[3,4], V Malvezzi[3], F Acernese[5,6], F Barone[5,6], G Giordano[5], R Romano[5,6], M Punturo[7], R De Rosa[6,8], P Calia[9] and G Loddo[9]

[1] Università di Roma *Sapienza*, Roma, Italia
[2] INFN - Sezione di Roma, Roma, Italia
[3] Università di Roma *Tor Vergata*, Roma, Italia
[4] INFN - Sezione di Roma *Tor Vergata*, Roma, Italia
[5] Università degli Studi di Salerno, Fisciano (SA), Italia
[6] INFN - Sezione di Napoli, Napoli, Italia
[7] INFN - Sezione di Perugia, Perugia, Italia
[8] Università di Napoli *Federico II*, Napoli, Italia
[9] I.G.E.A. S.p.A., Lula (NU), Sardegna, Italia

E-mail: fulvio.ricci@roma1.infn.it

Received 16 January 2014, revised 21 March 2014
Accepted for publication 1 April 2014
Published 6 May 2014

Abstract

To improve the sensitivity of the future generation of gravitational wave interferometers in the frequency range around 1 Hz it is necessary to decrease the seismic and Newtonian noise affecting the detector performance. This goal is achieved by installing the experimental apparatus in an appropriate underground site, where the Rayleigh surface wave of the microseismic motion should be attenuated. Here we report the results of an experimental campaign devoted to a long term characterization of one of the potential sites for the construction of a third generation of gravitational wave detector: the former mine of Sos Enattos (Sardinia, Italy). We analyzed the seismic stability within the low-frequency sensitivity band of a third generation gravitational observatory and the correlation between the microseismic band and the weather conditions, in particular focusing on the Tyrrhenian sea status.

Keywords: gravitational wave detectors and experiments, surface and body waves, oceanic crust seismology
PACS numbers: 91.30.Ye, 04.80.Nn, 91.30.Fn

(Some figures may appear in colour only in the online journal)

1. Introduction

The second generation of interferometric gravitational wave (GW) detectors Advanced LIGO and Virgo, [1–4] and KAGRA [5], the new interferometer under construction in Japan, will show a sensitivity improved roughly by a factor of ten with respect to the initial interferometers, which is expected to guarantee the detection of the signals generated by astrophysical sources starting from the science runs of the 2016–2018 biennium. However, the expected signal-to-noise ratio (SNR) of these detections is too low for precise astronomical studies of the GW sources and for complementing optical and X-ray observations in the study of fundamental systems and processes in the Universe. For this reason the investigation of a new design for the third generation of detectors is already started and led to the Einstein Telescope (ET) project [6, 7]. With a considerably improved sensitivity this new machine will open the era of routine GW astronomy [8].

Several limitations of the technologies adopted in the advanced interferometers must be overcome in order to build a third generation GW observatory with a significantly enhanced sensitivity. In particular, to enlarge the detector bandwidth in the range of 1 Hz, where interesting GW signals emitted by rotating neutron stars can be detected, a further reduction of the seismic noise effects with respect to the second generation detectors is needed. In the Virgo detector the seismic noise is attenuated by suspending each mirror to a long chain of several vertical and horizontal oscillators of nearly equal frequency ν_0 [10] [9]. In this way we reduce the amplitude of vibrations of frequency ν at the suspension point by a factor $(\nu/\nu_0)^{-2}$ at each stage. The goal of extending the detector bandwidth at lower frequencies implies to decrease both ν_0 and the seismic noise at the input of the suspension system [10]. Moreover, mass density fluctuations produced by the seismic motion also induce a stochastic gravitational field, which shunts the suspension and couples directly to the mirrors of the interferometer: it is the so-called *Newtonian noise* (NN) [11, 12].

The GW Japanese group suggested overcoming the limit due to the seismic and NN by constructing the interferometer in an underground site [13], where the Rayleigh surface waves are attenuated. These waves are always present at each point of the Earth's surface, and both the upper and deeper parts of the crust are constantly involved in their vibrations [14]. The heterogeneities of the Earth's crust influence the spectrum of the low frequency microseismic field, decreasing or increasing the spectral amplitudes at a specific frequency ν as a function of the depth of a heterogeneity and the velocity of the fundamental mode of the Rayleigh waves [15].

Moreover, several other causes influence the structure and the intensity of the spectrum of the ground motion, depending on the frequency range considered. The classification discriminating between low ($\nu < 1$ Hz) and high frequencies ($\nu > 1$ Hz) approximately corresponds to the distinction between natural microseisms and microtremors of anthropogenic origin. The nature of the microseismic field is complex: it is represented by the interference of

[10] In the case of Virgo we have a series of six oscillators with $\nu_0 \sim 0.4$ Hz.

seismic waves of different types traveling in the form of separate trains of a finite length. The relative amount of each wave mode and amplitudes, initial phases and lengths of these trains fluctuate so that the microseismic vibrations must be treated as a random process.

The stationarity of the microseisms noise depends on their frequency range. In the frequency range 0.06–0.15 Hz the noise spectrum is stable for few hours or even days, and the spectral variations correlate well with meteorological disturbances above oceans, determining the so-called oceanic *primary* and *secondary microseisms* [16, 17]. The microseisms in the frequency range 0.1–0.3 Hz are mostly generated by sea surf and are less stable in time. Their generation is similar to that due to the oceans, but takes place in inland seas, and is related to smaller wavelengths. Finally, at higher frequencies the microtremors are mainly associated to either industrial and transportation activities or drastic weather changes (local wind gusts) [18, 19]. In this frequency range the temporal stability of the spectrum is even shorter.

The microseismic noise level reduces with depth, because its energy content is mainly transported by surface waves; in fact, these waves are attenuated by multiple reflections in waveguides present in the shallow layers of the earth's crust. The random wave propagation and its attenuation factor is a complicated phenomenon, which depends on the local geology. Moreover, given the non-stationary nature of this random process, a long term campaign of measurements is needed to qualify the seismic performance of a single site.

Studying the low seismic activity and the uniformity of the soil plays a dominant role in the site identification process that should end by qualifying the area hosting the new GW interferometer. This is a complex underground facility, which includes multi-kilometre tunnels housing the ultra high vacuum tubes of the interferometer.

The monitoring of the seismic motion is performed by installing seismic sensors, according to seismologic standards, in an underground location at least 100 m deep with respect to the surface level. The seismic data are also correlated to the meteorological variables qualifying the weather in the surrounding surface. The observation should last for at least 1 year in order to study possible seasonal effects.

Because of the high seismic stability and low population density, Sardinia appears immediately as an ideal location in Europe for an interferometer of third generation. As first option, we looked at a basaltic zone in the west area of the island, but the advantage of locating a huge GW underground laboratory in a zone not very far from a modern motorway, plus the possibility to rely on previous geological studies, pushed us to focus our attention more on the oriental zone of Sardinia.

In the following sections, after a detailed discussion of the geological characteristics of the site, we describe the experimental apparatus deployed in the mine, then we discuss the results of a long measurement campaign, which revealed that the Sos Enattos mine is a promising underground location compliant with the low seismic background requirements of a third generation GW interferometer ($5 \times 10^{-9}\ m/f^2$ for $f > 1$ Hz and 0.5 μm RMS below 1 Hz [4, 6, 7]).

2. The geology of Sardinia and of the Sos Enattos mine

Sardinia is a seismically quiet region located in the European tectonic plate, far from the edge of many fault lines. The island is constituted of an ancient continental landmass (the *Sardinia–Corsica block*), isolated and partially dismembered from its Alpine orogeny, which explains its low seismic activity. It is largely formed by rocks of the Paleozoic era or, to be

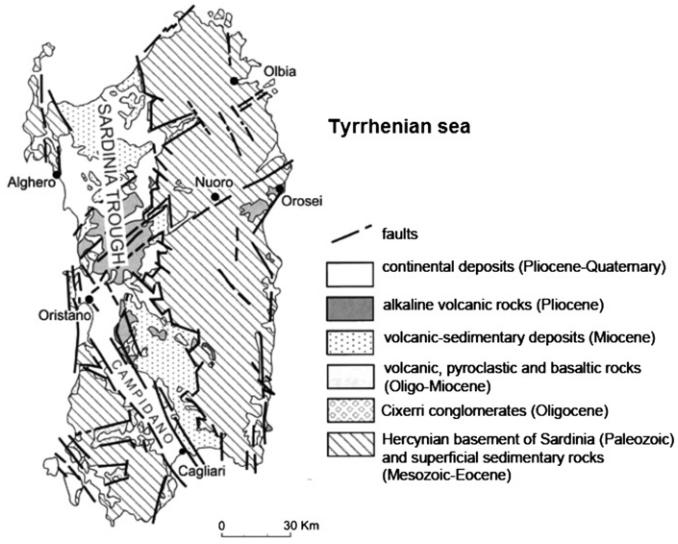

Figure 1. Geological map of Sardinia extracted from [20]. The *Hercynian* basement, formed during the *Paleozoic* era, is the oldest part of the island.

more precise, dating back to the Cambric and Silurian eras[11]. The island is classically divided into two geological domains, the *Sardinia Alpina* and the *Sardinia Hercynian* (i.e. Sardinia of the *Paleozoic era*, see figure 1):

- Sardinia Alpina occupies the western half of the island with the exception of the north-west (NW) and south-west (SW) extremities, characterized by the massive outcrops of Paleozoic and Nura–Sulcis Iglesiente.
- The Hercynian Sardinia extends in the eastern half of the island. It consists of Paleozoic metamorphic rocks with Hercynian deformation and a large intrusive complex of coal with a variable composition.

The central-eastern sector of the region is characterized by a rugged morphology in particular in the zone dominated by carbonate rocks. In this zone the Albo mountain stretches for about fifteen miles to the north-east (NE), and shows peaks over 1000 m. It is bordered on the south-east (SE) from the valley of Siniscola and to the west by a plateau of the Manno river. In the northerly direction, blocks degrade and show a stark contrast between the morphological rounded shapes developed in the metamorphism and those of granite, which are most rugged. Around Monte Albo territory there are few old mines, one of which is Sos Enattos.

The mine is located at ∼40 km N–NW from Nuoro in the land of the Lula village; it easily accessible via the motor way connecting the Bitti village to the *131bis* highway of Sardinia.

The area of Sos Enattos is hosted by Paleozoic metamorphic terrains, which are part of the broader *inclined roof* within the Hercynian granites of Sardinia. At the south edge of the area, this *roof* is covered by deposits of a carbonate platform due to a series of tectonic events at lower pressures during the Tertiary age. The tectonic transposition caused a significant homogenization of the original lithological types and a full distribution of each fossil, so that it is difficult to reconstruct the original stratigraphic sequence. However, the age of the

[11] The Sardinian basement, formed in the Paleozoic era, is one of the oldest geological formations of the central and southern Europe.

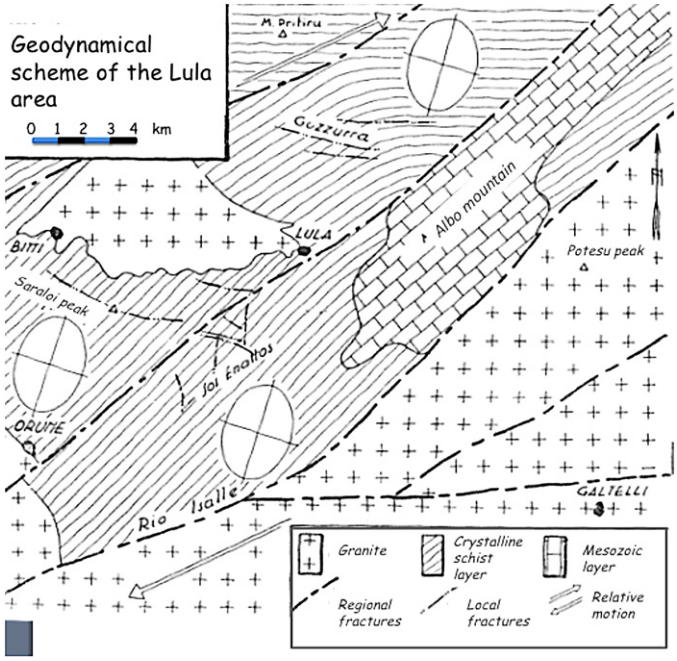

Figure 2. Geodynamical scheme of the land around Sos Enattos mine, in the northeast of the island (40°26′45″N - 9°27′24″E) [21].

crystalline–schist layer is definitely pre-Hercynian. This layer shows an uniform behavior with respect to mechanical stress, while the carbonaceous phyllite are more plastic than the other formations. In other words, we observe a bending of the carbonaceous layers and few fractures. The existing fractures have been studied with great attention because sometimes they are filled with minerals that can be exploited by the mining industry. Their location and characteristics are also interesting in our study because their spatial distribution influences the seismic wave propagation and reflection. In figure 2 we show the location of the fractures in the Lula territory.

The Sos Enattos mine, composed of schist rocks of sphalerite ([Zn,Fe]S) and galena (PbS), was exploited to extract lead and zinc. The mine history starts in 1864 and the end of its exploitation is dated 1996. The mine age (more than 100 years) guarantees the stability over the long term in the presence of long caverns in a deep underground environment. The site is managed by the I.G.E.A. S.p.A. company, which guarantees safe access to the mine.

Finally, we note that the Sos Enattos area is characterized by a very low anthropic activity: the population density in the Albo mountain area is low and in the Lula's territory is 10 habitants km^{-2}, a factor $\sim$7 lower than the mean value for Sardinia[12].

3. The experimental set-up

There are two main accesses of the Sos Enattos mine, both located well above the sea level (a.s.l.). The first access is a vertical pit equipped with a lift, and the second one is a long tunnel (called *Rampa Tupedddu* and oriented NNW) used to transport by car the workers with their

[12] The mean population density of the 28 nations of the European Union is 116 habitants km^{-2}.

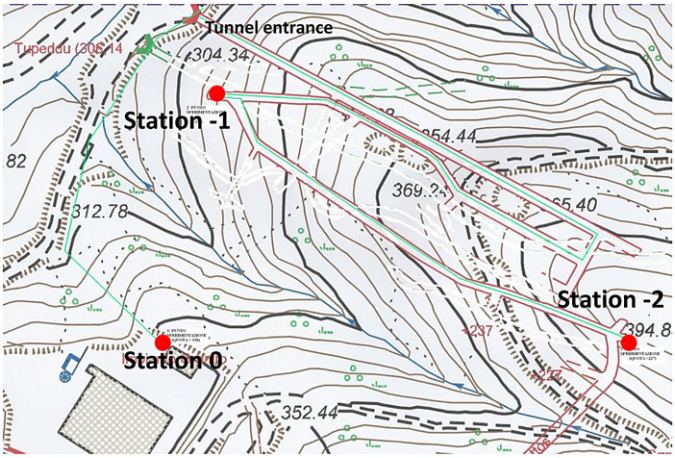

Figure 3. Location of the seismic stations in the Sos Enattos Mine (red dots). Courtesy of IGEA S.p.A.

mine tools in the past and tourists and scientists with their instrumentation in the present. The tunnel entrance is at +306 m a.s.l.

The experimental setup is presently distributed in three stations: the first one is at ground level while there are two seismic stations along the access tunnel of the mine. Both of them are connected by 1.3 km-long optical fiber links to the station at ground level to realize a three points data acquisition network, which allows remote access of the data measured and stored in the underground stations. Furthermore, the optical fiber link will allow future correlation and coherence measurement between the stations by using a distributed common timing, not implemented yet. In figure 3 we show a map of the mine tunnel, where the main access and the location of the seismic stations are marked by red dots.

The first monitoring station (named *station 0* in figure 3) is located at ground level (+338 m a.s.l.). This station is composed of a data acquisition system based on desktop PC equipped with a 32 channels 18 bit ADC board by National Instrument (NI-PCI 6289) and a weather station Vantage Pro II made by the US company Davis. The weather station includes a rain collector, an anemometer for measuring the velocity and the direction of the wind, a barometer and temperature sensors. Temperature and humidity sensors are enclosed in a radiation shield that protects them against solar and other sources of radiated and reflected heat, to improve the measurement accuracy.

The second station (named *station-1* in figure 3) is at +254 m a.s.l., 800 m from the entrance of the mine tunnel, at −66 m from the surface. A two layer wall, made of steel and polyurethane, is installed to reduce the acoustic noise and thermal drift. The environmental conditions are monitored by several temperature[13], humidity and atmospheric pressure probes. On a granite plinth anchored to mine bedrock and enclosed in insulation boxes, two pairs of uniaxial horizontal seismometers are installed. The first pair is East–West oriented and the other along the North–South direction. These are seismic sensors (UNISA FP), developed at the University of Salerno [22], which can operate in different configurations [23, 24]. In the *station-1* we use these sensors as seismometers in open feedback loop, and the pair permits to cross-correlate the data, improving its quality. The sensors are calibrated at resonant

[13] The thermal excursion in one year of observation, measured near the seismic sensors, is ±1.0 °C and the mean temperature is 19 °C.

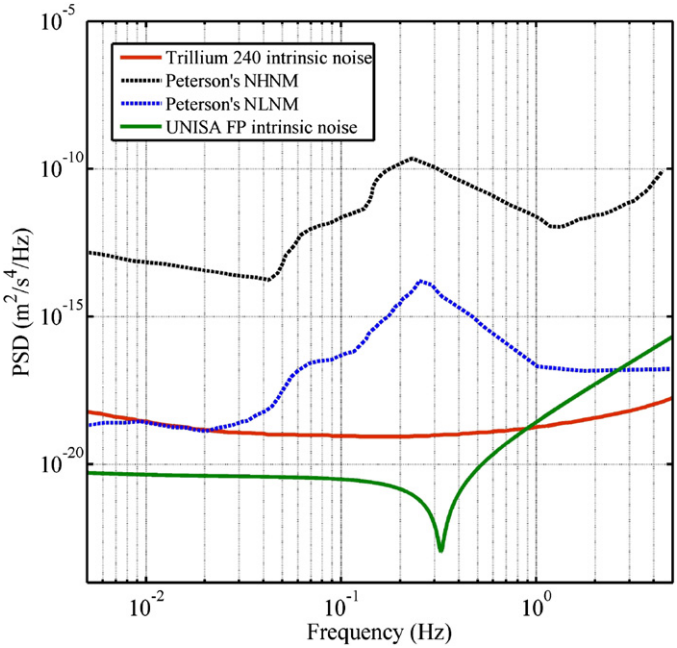

Figure 4. Comparison of the intrinsic noise spectra of the Trillium 240 and of the sensor made by the university of Salerno (UNISA FP) with the high (NHNM) and low (NLNM) noise curves of the Peterson model. The curves are power spectral densities of the acceleration noise measured in $m^2\ s^{-4}\ Hz^{-1}$.

frequency of ∼250 mHz. The read-out configuration is based on an optical lever, which allows the achievement of a high sensitivity in the frequency range 0.01–10 Hz (see figure 4). The sensor outputs are sent to a data acquisition system, based on two desktop PCs equipped with 32 channels 18 bit ADC boards (NI-PCI 6289 by National Instrument), where the signals are sampled at 10 kHz, with an antialiasing filter applied at 100 Hz. All the instrumentations, laser sources and DAQ PCs are connected to UPS powered buffer battery system through large inductive chokes to guarantee either power supply stability and a low electromagnetic noise.

The deeper seismic station, named *station-2* in figure 3, is located at +227 m a.s.l., 1100 m far from the tunnel entrance and −111 m from the surface. The sensor insulation and installation followed the same procedure described above for the other underground station, with the construction of two insulation walls delimiting two instrumental chambers along the cave.

Here the sensor is a tri-axial seismometer *Trillium 240* by Nanometrics Inc. [25], shielded from air currents and temperature fluctuations by means of a thermal shield. In addition, the system is covered by a second box made of wood with the inner walls padded with 5 cm polystyrene slabs.

The Trillium 240 has a symmetric triaxial arrangement of the sensing elements. The use of three identical axis elements ensures the same frequency response for vertical and horizontal outputs; it guarantees true orthogonality of the three outputs and a minor dependence of its response to rapid changes in temperature. The sensor is oriented in such a way that the X-output of the seismometer is proportional to the East–West movement of the ground, while Y is related to the North–South direction and Z to the vertical movement. The input–output transfer function of each channel has a frequency response flat from 5 Hz to few mHz and it rolls off at 40 dB/decade below the lower corner frequency.

The sensor cable exits the seismometer enclosure at the base of the instrument: it runs loosely from the inner to the outer chamber of the cave, preventing the vibrations from being transmitted along the cable. In the outer chamber of the cave the data acquisition system *Taurus* made by Nanometrics Inc. [26], collects and stores the data in the local memory. The overall (Trillium 240 + Taurus) system sensitivity is given by $S_T = 1.196 \times 10^3$ V m^{-1} s^{-1} with a nominal $\pm 0.5\%$ precision. The Trillium analogue output is sampled at 30 kHz and an antialiasing filter is applied at 40 Hz. Moreover, a digital filter of 141 dB attenuation is applied. The *Taurus* is connected to the local Ethernet network, so that it is possible to monitor the data acquisition process via the computer located in the surface station.

All the seismic sensors installed in the site were synchronized with the GPS signal before the installation in the underground stations, and their calibration was checked with a comparative measurement at INGV (Italian institute of geophysics and volcanology). In order to verify the significance of our seismic noise measurement, we compared the typical noise curve of the Trillium 240 seismometer and that of the sensor made by the university of Salerno with the Peterson curves [27] related to the new low-noise model (NLNM) and new high-noise model (NHNM) (see figure 4).

It is evident that both kind of sensors are suitable for monitoring microseismic noise, even below the NLMN limit, in a wide interval of the frequency bandwidth.

4. Environmental measurements

The seismic noise reduction around 1 Hz is a necessary condition to qualify the Sos Enattos site for a new GW underground installation. However, as we stated before, we also need to study the low frequency part of the spectrum, characterizing its non-stationary features. The noise in the frequency band below 1 Hz is the major contribution to the total root mean square (RMS) motion of the GW mirror. This quantity is crucial to define the feedback control loops, for locking the GW interferometer at the working point: in practice a high RMS value is an important limiting factor of the feedback dynamic. During the operation of the first generation of GW detectors we noted that the meteorological status of the site influences the detector performance. In particular, in presence of bad weather the RMS value of seismic motion in the frequency band below the mirror suspension cut-off, increase. As a consequence the dynamics of the feedback control loop of the mirror suspension [4, 7] is limited and it saturates more often: in this case the mirror position cannot be controlled (i.e. the interferometer *unlocks*) reducing the detector duty cycle. This behavior is observed mainly during windy days and is attributed in part to the random stress applied by the wind to the buildings hosting the interferometer mirrors.

In an underground laboratory this effect should be reduced but, since the requirement of new interferometer is to achieve a displacement sensitivity an order of magnitude higher than that of the advanced detectors in the observation bandwidth and an RMS < 0.5 μm below 1 Hz, we still need to verify how the seismic noise can be affected by the weather change. For this reason, we monitored continuously the weather variables at the mine entrance.

The weather in Sos Enattos is rather stable: in figure 5 we show the cumulative distribution of the wind velocity monitored during the winter and spring time (from November 2012 to July 2013).

The plot shows that for the 50% of the time the wind is in practice absent: the wind velocity is below 0.5 m s^{-1} and for the 99% the site is hit just by a light or a moderate wind increasing up to a velocity of 4 m s^{-1} (a moderate breeze).

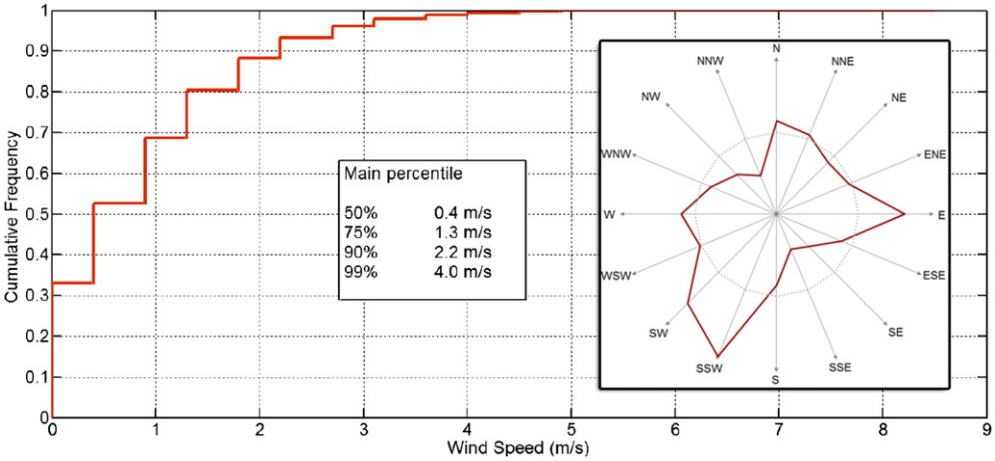

Figure 5. Cumulative distribution of the wind velocity. In the box we report the diagram of the wind direction. The data is taken from more than six months of observation.

Table 1. List of the variables derived by the *Nettuno* model provided by CNMCA.

Significant height of combined wind waves and swell (m)
Mean wave direction (deg)
Mean value of the wave frequency (Hz)
Wind speed (m s^{-1}) (10 m inshore space resolution)
Wind direction (deg) (10 m inshore space resolution)
Wave frequency of the highest peak in one-dimensional spectrum (Hz)
Coefficient of drag with waves
Mean sea level u component of wind (m s^{-1})
Mean sea level v component of wind (m s^{-1})

In the same figure we also report the diagram of the wind direction. Here the screen effect due to the orientation of the Albo mountain, the 20 km long barrier extended in the NNW–SSE direction, is evident.

As we will show in the next section, the meteorological status of the sea is an other important element to be considered in connection with the seismic activity of the mine site. The most common measuring devices of the sea status are based on the record of both vertical and horizontal accelerations of a floating buoy and pressure in the water column. Nowadays, satellite observations are routinely used, based mainly on techniques such as altimetry and synthetic aperture radar imagery. Moreover, since the late 1950s numerical wave models have been developed inferring also the spectral decomposition of the sea state and the propagation direction of each wave component. The surface of the sea is discretized in a number of points, which are separated by 100 km for a global scale prevision, but the inshore model resolution may be only a few meters apart. *Nettuno* [28] is the wind-wave forecasting system with the highest model computational resolution currently operating in the Mediterranean sea: 7 km (wind) and 4–5 km (waves) offshore resolution, and 10 m inshore resolution. It is based on the regional (WAM) and nearshore (SWAN) wave models [29, 30] and allows one to describe with great accuracy the evolution and breakdown of the fields along the coasts in a broad frequency spectrum. The model output variables (reported in table 1) has been calibrated and validated using data taken in-situ and from the EnviSat Radar Altimeter observations both in the Mediterranean sea [31] and in the Atlantic ocean [32].

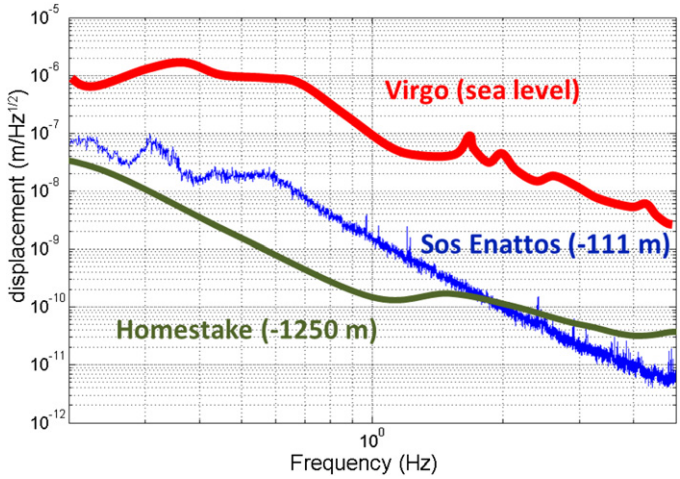

Figure 6. Displacement noise spectral linear density measured along the vertical direction in the Sos Enattos mine with a Trillium 240 seismometer, compared to those measured near the North building of the Virgo interferometer in Cascina (Pisa, Italy) with Kinemetrics FBA ES-T, and in the former mine of Homestake (Lead, SD - USA) with a Trillium 240 seismometer. Each instrument was calibrated independently and all the spectra were taken in similar meteorologic condition.

Table 2. The four points chosen to monitor the sea status: position, sea depth and distance from Sos Enattos (*Rampa Tupeddu* tunnel entrance).

Point	Coordinates (latitude and longitude)	Depth (m)	Distance (m) (from Sos Enattos)
A	40°32′60.00″N 9°48′00.00″E	<10	31308
B	40°27′00.00″N 9°48′00.00″E	<10	29112
C	40°32′60.00″N 9°56′60.00″E	155	43416
D	40°27′00.00″N 9°56′60.00″E	134	41840

At each of these points the program manages the evolution of the energy of all the spectral components. *Nettuno* uses 36 directions and 30 wave frequencies between 0.05–0.793 Hz. This means that at each point of the sea grid we are dealing with 36 times 30 variables that have to be evolved.

On the base of a formal agreement between the University of Roma 'Sapienza' and the national meteorologic center of the Italian Air Force (CNMCA), we have access to the several output values, updated every three hours by the *Nettuno* model.

These data are collected in four different point of the Tyrrhenian sea: two of them are near the oriental cost of the Sardinia, while the others are ∼10 km far from it (see table 2).

5. Seismic measurements

In order to demonstrate the potential gain in sensitivity for a GW interferometer built in Sos Enattos, we compare in figure 6 three spectra taken in similar meteorological conditions. The first one is the displacement noise spectrum measured near the north building of the Virgo interferometer using Kinemetrics FBA ES-T. The second curve is one of the noise displacement spectrum measured by the Trillium 240 located in the deepest station of the Sos Enattos mine.

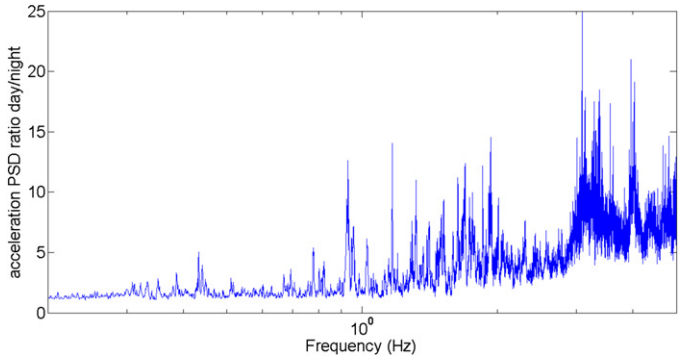

Figure 7. The ratio between 12 h-averaged day and night seismic noise PSDs at Sos Enattos, obtained from the data measured on May 2013; the floor level increase due to the anthropic noise mostly affects the analyzed band above ∼1 Hz.

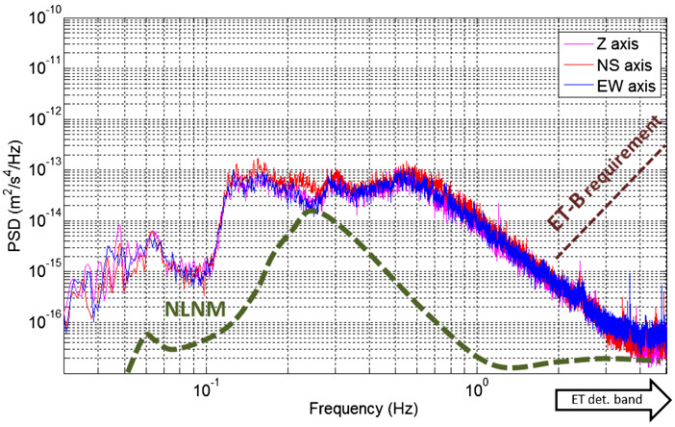

Figure 8. The PSD of the acceleration measured in the Sos Enattos mine with a Trillium 240 seismometer during a day with optimal meteorologic condition. The dashed lines represents the New Low Noise Model [27] and the seismic requirement for the ET [7].

The third one shows the displacement noise spectrum, measured with another Trillium 240 seismometer, installed ∼1 km depth from the surface in the former gold mine of Homestake (Lead, SD-USA).

In the lowest frequency range the Homestake spectrum falls below that of Sos Enattos. At 1 Hz the noise reduction with respect to the Virgo site at ground level is more than a factor 50. At higher frequency (in the ET bandwidth) the curves related to Sos Enattos and Homestake are inverted. We explain this behavior as due to the absence of industrial activity in the Monte Albo zone.

However, a contribution of the anthropic activity to the Sardinia mine spectrum is still present. To enlighten this effect, we selected one month of data (May 2013) and we computed the ratio between the spectra taken during the day and the night. In figure 7 we show the ratio between the daytime and the corresponding nighttime spectra in the 0.2–5 Hz band, averaged over 30 days: the increase of the floor level during the day mostly affects the frequencies above 1 Hz.

In figure 8 we show the power spectral density (PSD) of the acceleration measured in the Sos Enattos mine in the full frequency range of the Trillium 240.

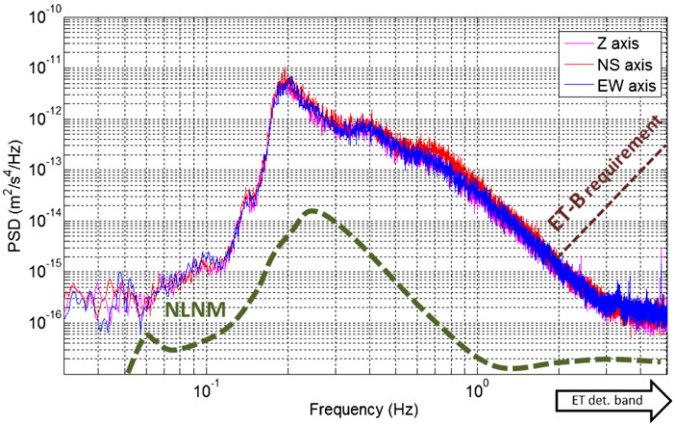

Figure 9. The PSD of the acceleration measured in the Sos Enattos mine with a Trillium 240 seismometer during a stormy day of winter. The dashed lines represents the New Low Noise Model [27] and the seismic requirement for the ET [7].

This spectrum has a shape similar to the reference curves shown in figure 4. The Peterson model was derived using data collected in 75 seismic stations equipped with both surface and borehole sensors (100–340 m depth) distributed worldwide.

We observe peaks of the power spectrum clustered in the interval of 0.03 and 0.1 Hz. In this frequency range, the noise classified as *microseismic*, is due to non-local causes, and generally it depends on large-scale meteorological conditions[14].

Above 0.1 Hz a band resulting from the envelope of several broad peaks is present. During the long period of the monitoring process, we observed that this part of the spectrum shows a non-stationary behavior. In a stormy day the broad band grows up almost two orders of magnitudes as shown in figure 9, while in the frequency range above 1 Hz the change of PSD value is just a factor two.

Apparently the noise increase in the frequency range 0.1–1 Hz seems to be correlated to the wind velocity and the lowering of the atmospheric pressure. The effect is more evident if we focused our analysis on the data taken at the end of autumn, a period of time characterized by unstable weather conditions. In figure 10 we report the history plot of the wind vector velocity measured at the mine entrance versus time and the corresponding RMS acceleration noise in the mine, integrated in the frequency range 0.1–3 Hz. An analogues plot is shown in figure 11 for the atmospheric pressure.

In order to clarify if the wind is the direct cause of the seismic noise increase in the deep mine, we selected some periods of the data for which there were a significant variability of the local wind speed. As example, here we report just the data collected during three days of observation. The corresponding history plots of this time period are shown in figures 12 and 13. In the first one the wind velocity increase is delayed with respect to the seismic noise. However, in the same plot we note a wind velocity peak at the time $t_w = 12$ h, which could be interpreted as a precursor of the systematic worsening of the meteorological conditions. The precursor appears nearly 6 h before the seismic noise increase. The time lag between the local wind and the seismic noise increase was observed also in other data samples.

[14] At lower frequencies, out of the Trillium 240 bandwidth, the Earth ground experiences the large external forces due to the gravitational attractions of the Moon and Sun. The tidal motion has amplitudes of about 0.5 m with respect to the center of the Earth, but it occurs in the frequency range of 10^{-5} Hz and determines a quasi-coherent movement of the interferometer test masses. The quadrupolare GW signal will be detected at much higher frequencies and the residual tidal effect due to the tide anisotropy is easily compensated by a feed-forward system [33].

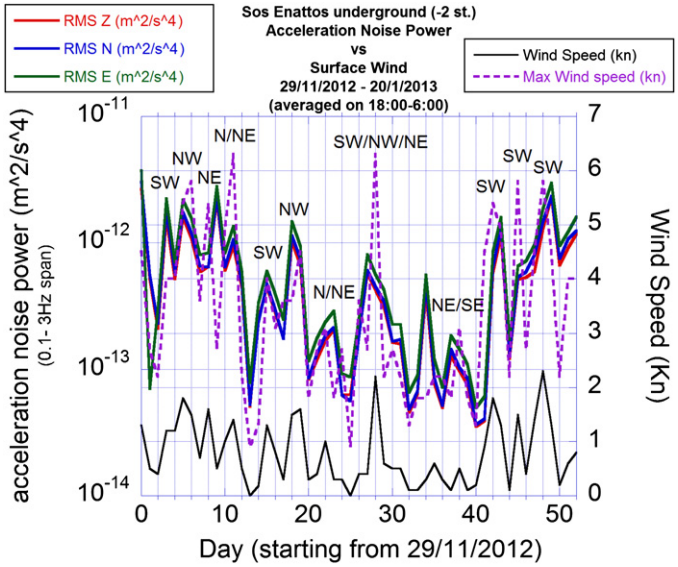

Figure 10. Wind speed ($1\ kn \approx 0.514$ m s^{-1}) measured at the mine entrance versus time and the corresponding RMS acceleration noise in the mine integrated in the frequency range 0.1–3 Hz.

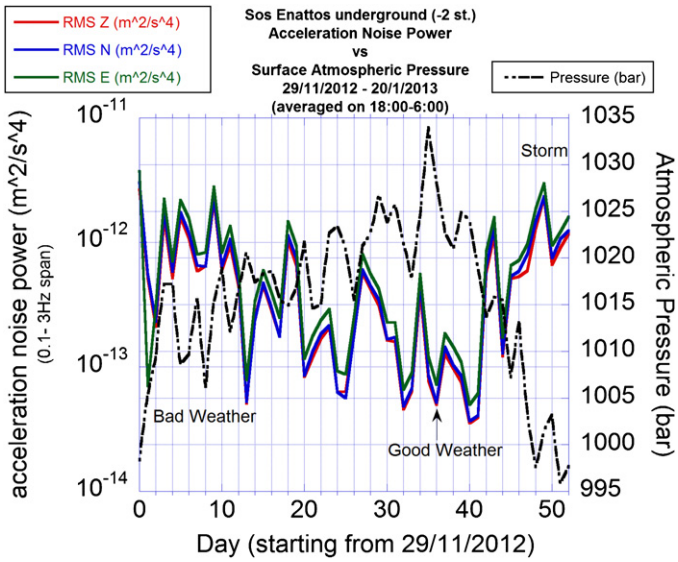

Figure 11. Atmospheric pressure measured at the mine entrance versus time, compared to the RMS acceleration noise integrated in the frequency range 0.1–3 Hz.

In figure 13 the pressure drop anticipate the seismic noise increase of nearly 10 h and it seems to be correlated with the 12–13 h peak of the wind velocity spectrum, the precursor of the weather worsening.

The delays of several hours rule out a direct relation between the wind stress on the rocks of the hill hosting the mine and the seismic noise. Instead the correlation between the sea wave height and the seismic motion in the mine is more evident in figure 14.

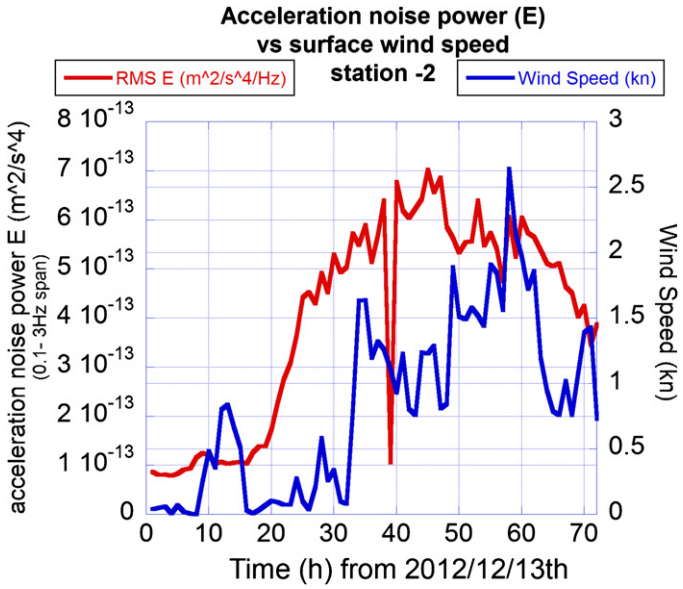

Figure 12. RMS acceleration noise computed in the frequency range 0.1–3 Hz and wind velocity (1 $kn \approx 0.514$ m s^{-1}) during three days of observation. The wind velocity increase is observed around the time $t_w \sim 30$ h, delayed to the respect of the corresponding seismic noise increase ($t_s \sim 20$–22 h). In the same plot we note the existence of a wind velocity peak at the time $t_w \sim 12$–13 h, which is interpreted as a precursor of the systematic worsening of the meteorological condition. The precursor peak is nearly 8–10 h before the seismic noise increase.

Table 3. Main microseismic peaks observed in Sos Enattos. A tertiary peak appears sometimes, maybe produced by standing waves in another sector of the Mediterranean sea.

Peak	Source	Mechanism	Frequency (Hz)
Primary	Oceans	Pressure variations, wave impact on shores	6–9×10^{-2}
Secondary	Oceans	standing wave	0.12–0.20
Primary	Tyrrhenian sea	Pressure variations, wave impact on shores	0.08–0.23
Secondary	Tyrrhenian sea	standing wave	0.16–0.46
Tertiary	Mediterranean (?)	standing wave or local resonance	0.27–0.63

Generally the sea status is strongly correlated with the wind velocity. To increase our confidence in the assessment that the seismic noise increase is due to the propagation of the seismic waves in the solid crust below the Tyrrhenian sea, we analyze the spectral composition of the seismic noise. In figure 15 we show the result of our analysis: the various broad peaks of the spectra are fit with a gaussian function to derive their central frequency, maximum amplitude and half a maximum width. The lowest frequency peaks of the spectrum are attributed to the primary and secondary oceanic microseisms while the two other peaks at higher frequencies are assigned to the primary and secondary microseisms [16, 17] produced by wind waves and swell in the Tyrrhenian sea. The typical frequency ranges of these peaks are reported in table 3: note that primary and secondary frequencies are in harmonic relationship

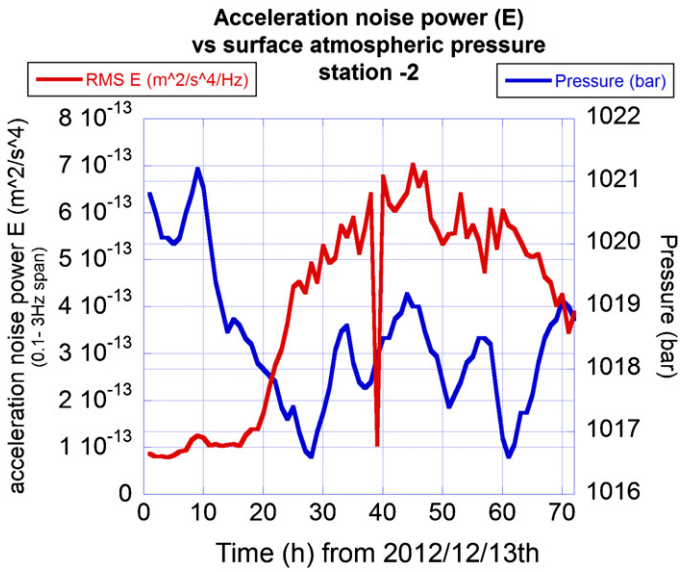

Figure 13. RMS acceleration noise computed in the frequency range 0.1–3 Hz and atmospheric pressure during three days of observation. The pressure drop anticipates the seismic noise increase of nearly 6 h. This remark emphases the interpretation of the 12 h peak in the wind velocity spectrum (see figure 12) as precursor of the systematic worsening of the meteorological condition.

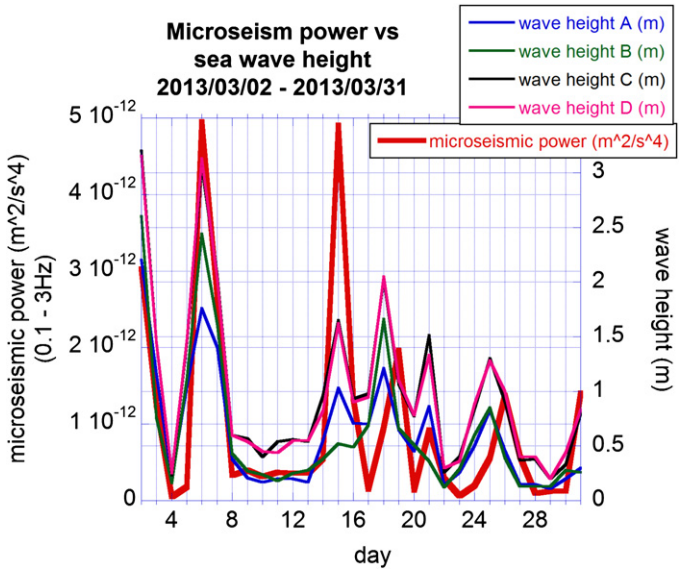

Figure 14. RMS acceleration noise computed in the frequency range 0.1–3 Hz and atmospheric pressure compared to the wave height provided by the Nettuno meteorological model at the points listed in table 2 for a period of about one month of observation.

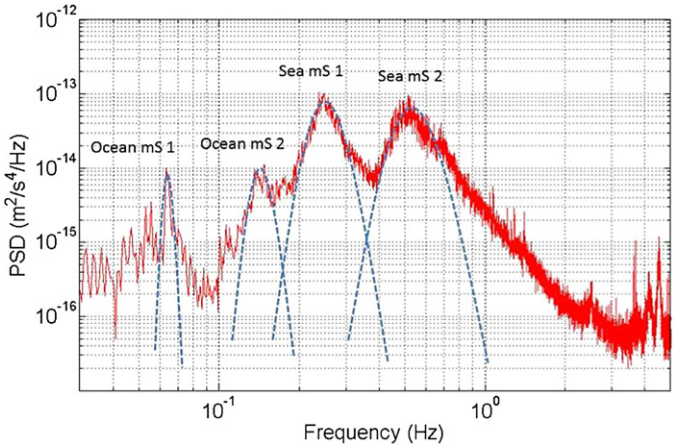

Figure 15. Spectral decomposition of the seismic noise spectrum measured in the deepest station of the Sos Enattos mine. The lowest frequency peaks are attributed to the primary and secondary oceanic microseisms (*Ocean mS* 1 and 2) while the two other peaks at higher frequencies are related to the primary and secondary microseisms generated in the Tyrrhenian sea (*Sea mS* 1 and 2).

since the secondary standing waves are produced from the interference between primary incident waves and those reflected back by the coast.

To assess this identification we plot the height of combined wind-generated waves and swell as function of the time, at the sea points C and D (see table 2), and the corresponding spectral acceleration noises in the mine integrated in the frequency ranges 0.06–0.18 Hz, 0.18–2 Hz and 0.06–2 Hz. This analysis method permits us to evaluate the sea and the ocean contribution to the seismic noise increase (see figure 16).

Moreover, we considered the same time period of observation and again just the sea status data related to the sea point C and D (∼10 km far from the coast) corresponding to a wave height range $0.3\,\mathrm{m} < h < 1.7\,\mathrm{m}$. The choice of the height interval is motivated by the empirical assumption that for $h < 0.3$ m waves in C and D, the seismic peak should be caused mainly by higher waves in other areas of the Mediterranean sea. For $h > 1.7$ m the sea peak shifts at lower frequencies overlapping the oceanic spectral structures.

Then, we correlate the frequency value of the highest peak in the shallow-water[15] wave spectrum, provided by the *Nettuno* model for the sea points C and D, and the frequency of the primary sea-generated peak in the seismic spectrum, measured in coincidence in the mine. The correlation plot is shown in figure 17.

Applying a two tail t-test to the correlation values $R_C \simeq 0.71$ (sea point C) and $R_D \simeq 0.68$ (sea point D), we obtain probabilities $p = 8 \times 10^{-5}$ and $p = 3 \times 10^{-4}$ for the null-correlation hypothesis. We point out that the correlation plot has been produced using synchronized data[16] (zero time delay). This is justified by the distance between the coast and Sos Enattos (see table 2) and the geology of this region of Sardinia. In fact, we expect a propagation time for the seismic perturbation from the sea to the mine of the order of tens of seconds, a time delay too short to be appreciated, given the 3 h sampling rate of the *Nettuno* output variables.

[15] The sea points C and D are on the border of the continental plate and moving far from there the sea depth falls down to more than 1000 m.

[16] The DAQ system was synchronized with the GPS timing before the sensor installation and then checked roughly on daily basis. The possible desynchronization during one year of measurement is negligible since the *Nettuno* model provides a value sampled every three hours.

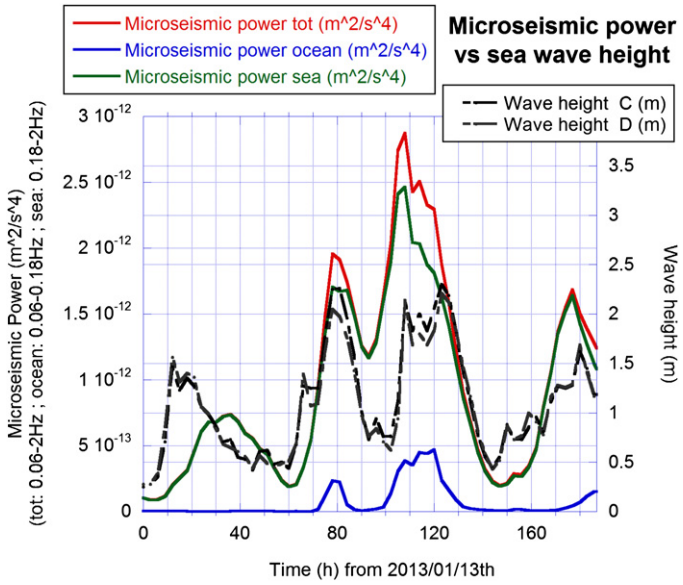

Figure 16. The height of waves, measured at the off-shore points C and D, versus time and the corresponding spectral acceleration noises in the mine integrated in the frequency ranges 0.06–0.18 Hz, 0.18–2 Hz and 0.06–2 Hz.

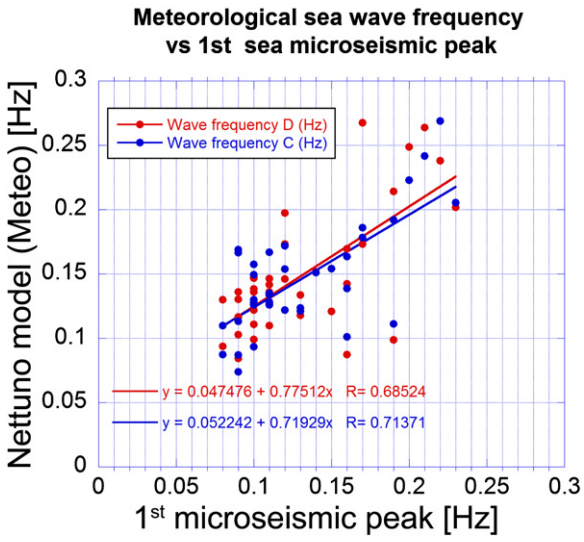

Figure 17. Frequency of the highest peak on the sea wave spectrum versus the frequency of the primary sea-generated peak (*Sea ms1*) on the seismic spectra measured in the Sos Enattos mine, obtained from the same data sample (about eight days) of figure 16.

In conclusion, the correlation between the trends of the microseismic activity and the Tyrrhenian sea wave height, together with the frequency correlation between the primary sea-generated microseismic peak and main wave peak provided by the *Nettuno* meteorological model, indicate the close link of cause and effect between the local microseismic variations and the sea status. Meteorological forces, such as wind and air pressure, produce wind-generated waves, which transform into swell, transferring their energy to the continental crust

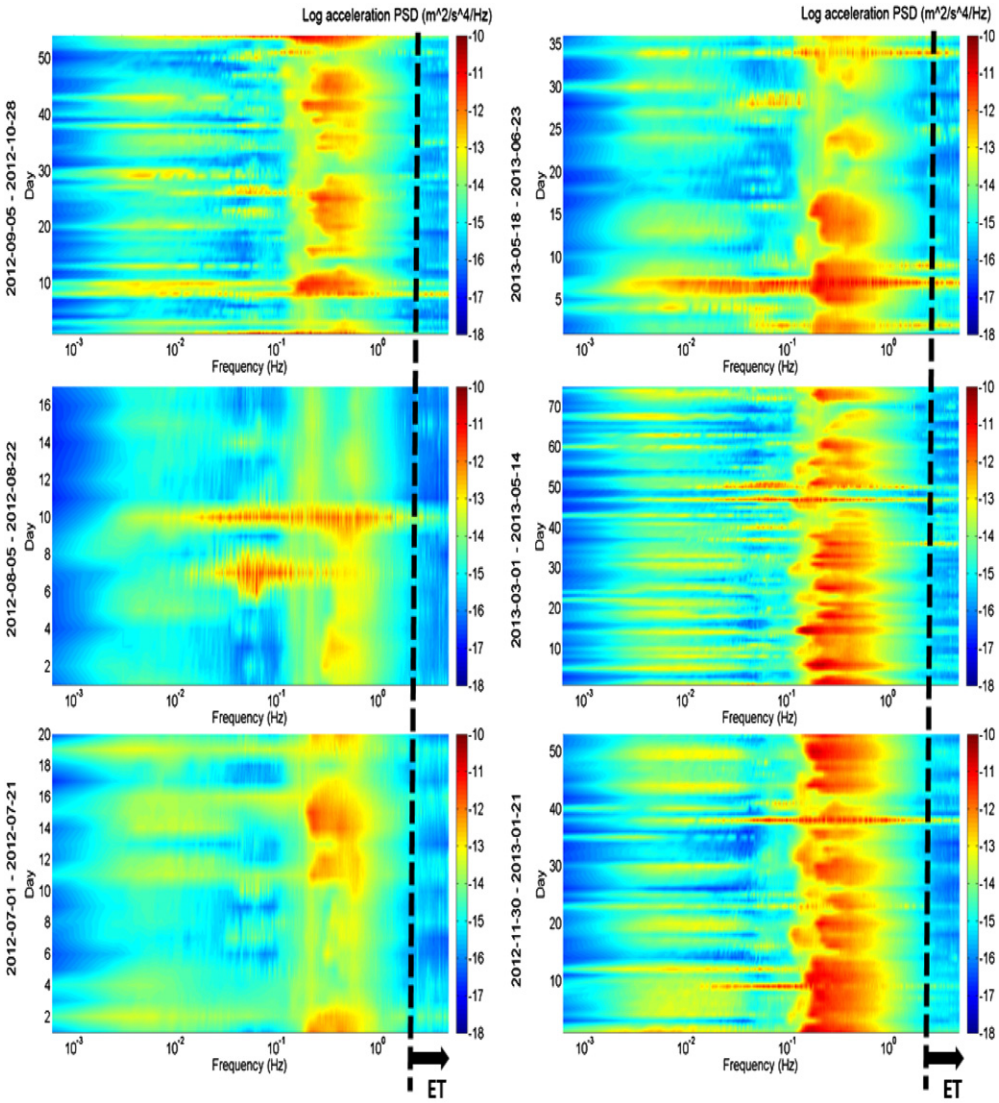

Figure 18. Ensemble of the power spectral densities of the acceleration noise measured during the observation period; the dashed line represents the lower limit of the ET detection frequency band. The seasonal effect is evident in the microseismic frequency range.

as seismic waves through the primary and secondary wave mechanisms. The observed time delay between the local wind and the seismic noise increase can be explained as a consequence of the dissipative processes determining the interaction between the wind and the sea surface [34–36], so that the generation of wind waves is not instantaneous.

6. Long term characterization and conclusion

The results of the seismic monitor of Sos Enattos mine is summarized in the three-dimensional plots of figure 18. Here we present the spectra taken during the long observation period lasting

from July 2012 to July 2013 in function of the time, subdivided in six periods of continuous data samples. Each spectrogram is computed by averaging over 24 h the data collected in time intervals of 7 min. The color scale is related to the power spectrum intensity.

In these plots it is rather evident that the two frequency intervals 0.02–0.05 Hz and 0.1–1.0 Hz are the most affected by a non stationary behavior. However, the variations of the noise level also during the stormy days are well below the feedback requirement of the mirror control system for both Advanced Virgo and a third generation of GW interferometer (see section 1). In addition, above 1 Hz, all the noise spectra collected during one year are fully compliant with the ET noise requirements [6, 7].

Moreover, the geological stability of the region, the low microtremor noise registered in the mine, due to the absence of industrial activities in the vicinity, and in general the whole profile of the noise acceleration spectrum close to the NLNM curve of Peterson in a large frequency range, bring us to the conclusion that the Sos Enattos mine is a good candidate for the construction of the ET.

Acknowledgments

The authors thank the authorities of Regione Sardegna and the direction of IGEA S.p.A. for access to the site of the Sos Enattos mine. In particular we wish to thank all the staff members of the mine for their crucial technical support. Data concerning the sea condition are provided by the *Servizio Meteorologico dell'Aeronautica Militare*. We are grateful to Col M Ferri, T Col R Tajani and Gen P Pagano for their support. This work has been supported by the research grant of the University of Rome *Sapienza* C26A113CE2 and by the Istituto Nazionale di Fisica Nucleare.

References

[1] Acernese F *et al* 2012 Virgo, a laser interferometer to detect gravitational waves *J. Instrum.* **7** 1–124
[2] Grote H *et al* 2005 *Class. Quantum Grav.* **22** S193
[3] Abbott B *et al* 2004 *Nucl. Instrum. Methods* A **517** 154
[4] Accadia T *et al* 2012 *Advanced Virgo Technical Design Report VIR-0128A-12*
[5] Somiya K 2012 Detector configuration of KAGRA–the Japanese cryogenic gravitational-wave detector *Class. Quantum Grav.* **29** 124007
[6] Punturo M *et al* 2010 The Einstein telescope: a third generation gravitational wave observatory *Class. Quantum Grav.* **27** 194002
[7] Abernathy M *et al* 2011 Einstein gravitational wave Telescope conceptual design study *ET-0106C-10* http://et-gw. eu/etdsdocument
[8] Sathyaprakash B *et al* 2012 Scientific objectives of Einstein Telescope *Class. Quantum Grav.* **29** 124013
[9] Braccini S *et al* 2005 Measurements of the seismic attenuation performance of the Virgo superattenator *Astropart. Phys.* **23** 557–65
[10] Acernese F *et al* 2010 Measurements of the superattenuator seismic isolation by the Virgo interferometer *Astropart. Phys.* **33** 182–9
[11] Saulson P R 1984 Terrestrial gravitational noise on a gravitational wave antenna *Phys. Rev.* D **30** 732–6
[12] Beccaria M *et al* 1998 Relevance of Newtonian seismic noise for the VIRGO interferometer sensitivity *Class. Quantum Grav.* **15** 3339–62
[13] Miyoki S *et al* 2006 The CLIO project *Class. Quantum Grav.* **23** S231–7
[14] Becker M *et al* 2010 Improving the sensitivity of the future GW observatories in the 1 Hz band: Newtonian and seismic noise *Gen. Rel. Grav.* **10** 1–34
[15] Gorbatikov A V, Stepanova M Yu and Korablev G E 2008 Microseismic field affected by local geological heterogeneities and microseismic sounding of the medium *Izv. Phys. Solid Earth* **44** 577–92

[16] Longuet-Higgins M S 1950 A theory of the origin of microseisms *Phil. Trans. R. Soc. Lond.* **243** 1–35
[17] Cessaro R K 1994 Sources of primary and secondary microseisms *Bull. Seismol. Soc. Am.* **84** 142–8
[18] Fiori I, Holloway H and Paoletti F 2003 Studies of the 1–4 Hz seism *VIR-NOT-FIR 1390-251*
[19] Young C 1996 A comparison of the high-frequency ($f > 1$ Hz) surface and subsurface noise environment at three sites in United States *Bull. Seismol. Soc. Am.* **86** 1516–28
[20] Carmignani L *et al* 2004 The internal northern Apennines, the northern Tyrrhenian sea and the Sardinia–Corsica block *Geology of Italy: Special Volume of the Italian Geological Society for the IGC 32* pp 59–67
[21] Manca F *et al* 2009 Piano per il risanamento ambientale dell'area mineraria di 'Sos Enattos' *Relazione tecnica descrittiva - IGEA S.p.A.*
[22] Barone F and Giordano G 2011 Low frequency folded pendulum with high mechanical quality factor, and seismic sensor utilizing such a folded pendulum *International Application published under the patent cooperation treaty (PCT),* WO 2011/004413 A3, Patent Number 0001394612 (Italy, 2012)
[23] Acernese F, De Rosa R, Giordano G, Romano R and Barone F 2008 Mechanical monolithic horizontal sensor for low frequency seismic noise measurement *Rev. Sci. Instrum.* **79** 074501
[24] Acernese F, De Rosa R, Giordano G, Romano R and Barone F 2013 Low frequency/high sensitivity triaxial monolithic inertial sensor *Proc SPIE* **8893**
[25] Trillium 240 Seismometer User Guide by Nanometrics Inc. 2005
[26] Taurus Portable Seismograph User Guide by Nanometrics Inc. 2004–2007
[27] Peterson J 1993 Observation and modeling of seismic background noise *U. S. Geol. Surv. Open-File Rept.* **2** 93–322
[28] De Simone C, Torrisi L, Vocino A, Bertotti L and Cavalieri L 2010 *Riv. Meteorologia Aeronaut.* **70** 25-36
[29] Hasselmann S *et al* 1998 The WAM model a third generation ocean wave prediction model *J. Phys. Oceanogr.* **18** 1775–810
[30] European Centre for Medium-Range Weather Forecasts (ECMWF), ECMWF Wave Model http://ecmwf.int/research/ifsdocs/CY38r1/IFSPart7.pdf *IFS Documentation Cy38r1* 1–75
[31] Ardhuin F, Bertotti L, Bidlot J R, Cavaleri L, Filipetto V, Lefevre J M and Wittmann P 2007 Comparison of wind and wave measurements and models in the Western Mediterranean Sea *Ocean Eng.* **34** 526–41
[32] Gusdal Y, Carrasco A, Furevik B R and Sætra Ø 2011 Validation of the Operational Wave Model WAM at met.no - Report 2010 *Report of the Norvegian Meteorological Institute - Oceanography no. 14/2011, December 8*
[33] Acernese F *et al* 2004 The commissioning of the central interferometer of the Virgo gravitational wave detector *Astropart. Phys.* **20** 629–40
[34] Belcher S E and Hunt J C R 1993 Turbulent shear flow over slowly moving waves *J. Fluid Mech.* **251** 109–48
[35] Makin V K and Kudryavtsev V N 1999 Coupled sea surface-atmosphere model-1. Wind over waves coupling *J. Geophys. Res.* **104** 7613–23
[36] Kudryavtsev V N, Makin V K and Chapron B 1999 Coupled sea surface-atmosphere model-2. Spectrum of short wind waves *J. Geophys. Res.* **104** 7625–39